# Rotational excitation of HDO and $D_2O$ by $H_2$: Experimental and theoretical differential cross-sections

Gautam Sarma, Chung-Hsin Yang, Ashim Kumar Saha, David H. Parker, and Laurent Wiesenfeld'

Citation: The Journal of Chemical Physics **138**, 024314 (2013); doi: 10.1063/1.4772600
View online: http://dx.doi.org/10.1063/1.4772600
View Table of Contents: http://aip.scitation.org/toc/jcp/138/2
Published by the American Institute of Physics

# Rotational excitation of HDO and $D_2O$ by $H_2$: Experimental and theoretical differential cross-sections

Gautam Sarma,[1] Chung-Hsin Yang,[1] Ashim Kumar Saha,[1] David H. Parker,[1] and Laurent Wiesenfeld[2,a)]

[1]*Institute for Molecules and Materials, Radboud University Nijmegen, Nijmegen, The Netherlands*
[2]*IUJF-Grenoble 1/CNRS-INSU, Institut de Planétologie et d'Astrophysique de Grenoble (IPAG) UMR 5274, Grenoble F-38041, France*

(Received 24 September 2012; accepted 4 December 2012; published online 11 January 2013)

We present state-to-state differential cross sections (DCSs) for rotationally inelastic scattering of HDO by normal- and para-$H_2$ at collision energies of 580 $cm^{-1}$ and 440 $cm^{-1}$. (2+1) resonance enhanced multiphoton ionization is used to detect rotationally cold HDO molecules before collision and as scattering products, which occupy higher rotational states due to collision with $H_2$. Relative integral cross sections of HDO are obtained by integrating its DCSs measured at the same experimental conditions. Experimental and theoretical DCSs of HDO scattered by normal- and para-$H_2$ are in good agreement in 30°–180° range of scattering angles. This partial agreement shows the accuracy of the recently tested potential of $H_2O$–$H_2$, but now by using a completely different set of rotational transitions that are (unlike in $H_2O$), not forbidden by nuclear spin restrictions. Similar results are presented for $D_2O$ scattered by normal-$H_2$ at collision energy of 584 $cm^{-1}$. The agreement between experiment and theory is, however, less good for forward scattering of HDO/$D_2O$. A critical analysis of this discrepancy is presented. © *2013 American Institute of Physics*. [http://dx.doi.org/10.1063/1.4772600]

## I. INTRODUCTION

Water is one of the most important molecules discovered in the interstellar medium. Understanding the role of this molecule, in all its isotopic forms, is the subject of a massive effort of the recently launched Herschel Space Observatory.[1–6] HDO and, to a lesser extent, $D_2O$ have been specific targets of many observations whose goals are to determine the abundance and physical and chemical importance of water in astrophysical processes.[7–14] Abundance of water in the interstellar matter (ISM) varies greatly, with a ratio of density with respect to molecular hydrogen: $x(H_2O)$, up to $\sim 10^{-4}$ in some outflows of proto-stellar environments. Similarly, the ratio $x(HDO)/x(H_2O)$ is variable; a typical range is $10^{-3} \ldots 10^{-2}$, depending on the chemical history of the observed water.[15]

Microwave emissions from HDO and $D_2O$ are less absorbed in the terrestrial atmosphere than those of $H_2O$, and weak signal from these molecules can be detected even from ground-based telescopes. Detection of HDO in order to measure the D/H ratio has found many applications, as its spatial variation gives an indication of deuterium substitution by chemical reactions in the interstellar molecules.[16] Also, the presence of $D_2O$ is an example of the rich chemistry of polydeuterated species.[12,17]

Most observation of water rotational lines occur in emission against the radiation background. The collisional excitation of water molecules, mostly by $H_2$, the main neutral molecular gas, yields rotational level populations either at local thermodynamical equilibrium (LTE) with the main gas, or else out of equilibrium with both the molecular gas and the photon bath. In the LTE case, since the kinetic temperature is more often higher than the photon background, the spectral lines are seen in emission. In the non-LTE case, spectral lines are very often seen in emission, but masing or super cooling may also occur.[18] In all of those non-LTE cases, a precise knowledge of the rate of energy exchange between the kinetic energy of the $H_2$ gas and the $H_2O$ or HDO internal modes is a key ingredient in order to model the water gas and the ISM as a whole, because dipolar molecules are by far the best probes of the ISM. Knowing the exchange rates relies on the computation of the inelastic collision cross sections. These scattering calculations strongly depend on the accuracy of the potential energy surface for the interactions between molecules.[19] Recently, the Grenoble group has calculated quenching rates of all water isotopes by molecular hydrogen,[18,20] opening the possibility of fully employing and testing the water-hydrogen potential.

This paper is part of a series aimed at testing these quenching cross sections against experimental differential cross sections (DCSs), which are a very sensitive probe of the accuracy of the anisotropic part of the potential energy surface (PES). We have recently reported rotationally resolved state-to-state DCSs for $H_2O$ collisions with $H_2$, and He using a crossed beam machine combined with velocity map imaging (VMI)[21] detection. Experimental DCSs and total cross sections were in very good agreement with those derived from theory,[22–24] thereby in agreement with other experimental tests performed on the water-molecular hydrogen experiments.[25–28]

The paper is organized as follows. Section II outlines the rotational structure of HDO and $D_2O$ and the experimental

a)Electronic mail: Laurent.Wiesenfeld@obs.ujf-grenoble.fr.

 

setup. In Sec. III, we describe the method employed for theoretical calculations. Comparison of experimental and calculated differential and total relative cross sections for different rotational transitions of HDO/$D_2O$ scattered by $H_2$ are presented in Sec. IV, together with a discussion and conclusion.

## II. EXPERIMENT

### A. Rotational levels and collisional processes

$H_2$ comes into two spin modifications, the para state (total nuclear spin $I = 0$) and ortho state ($I = 1$). Ortho-$H_2$ has rotational states with odd quantum numbers ($J = 1, 3, \ldots$) while para-$H_2$ has even rotational states ($J = 0, 2, \ldots$). The rotational constant of $H_2$ is taken at 60.853 $cm^{-1}$, its average value for the ground vibrational state.[29] HDO and $D_2O$ being asymmetric tops, their rotational levels are labelled by $J_{K_aK_c}$, where $J$ is the total angular momentum and $K_a$, $K_c$ are the pseudo-quantum numbers giving the projections of $J$ on the principal inertia axes $a$ and $c$. For $D_2O$, the $b$ axis is along the $C_2$ symmetry axis, the $c$ axis is perpendicular to the molecular plane. For HDO, the $a$ and $b$ axes are tilted from the $\widehat{DOH}$ angle bisector direction by an angle of 21.11° towards the D atom.[30,31] Rotational constants are for $D_2O$ (resp. HDO), in $cm^{-1}$: $A = 15.4199$ (23.4139), $B = 7.2729$ (9.1033), $C = 4.8452$ (6.4062).[32] Reduced collision masses are 1.8313 (1.8225) amu.

HDO, the first molecule we report here, differs from $H_2O$ merely by a substitution proton/deuteron; however, it is essentially a different molecule from symmetry and structure points of view. The rotational states of HDO carry no peculiar spin selection rule. The HDO–$H_2$ PES is the same as the $H_2O$–$H_2$ PES, except for symmetry conditions fully taken into account as described in details in Ref. 30, and for non-Born-Oppenheimer effects neglected in the present approach. The $D_2O$ molecule is essentially identical to the $H_2O$ molecule, coming into two spin modifications. D being a boson (nuclear spin 1), the ortho and para species are inverted. For $D_2O$, $K_a + K_c$ even are ortho states, while $K_a + K_c$ odd are para states. The lower rotational levels of all three molecules, $H_2O$, HDO, and $D_2O$ are given in Fig. 1 where it is seen that energy order and even the relative spacing of the quantum states for each molecule is quite similar.

We present detailed studies of the following collision processes:

$$\mathrm{HDO}(J_{K_aK_c} = 0_{00}) + \mathrm{H_2}(J = 0, 2 \text{ or } 1) \rightarrow \mathrm{HDO}(J''_{K''_aK''_c}) + \mathrm{H_2}(J'' = 0, 2 \text{ or } 1) \quad (1)$$

and

$$\mathrm{D_2O}(J_{K_aK_c} = 0_{00} \text{ or } 1_{01}) + \mathrm{H_2}(J_2 = 0, 2 \text{ or } 1) \rightarrow \mathrm{HDO}(J''_{K''_aK''_c}) + \mathrm{H_2}(J'' = 0, 2 \text{ or } 1). \quad (2)$$

Rotational quantum states of HDO, $D_2O$, and hydrogen before collisions are indicated by unprimed $J$ values and the double prime symbol ($J''_{Ka''Kc''}$ or $J''$) indicates their final states after collision. The collision energies of the HDO–$H_2$ system are 440 $cm^{-1}$ and 580 $cm^{-1}$, while $D_2O$ scattered by $H_2$ is studied at a collision energy of 584 $cm^{-1}$. As no atom exchange is possible at these collision energies, the ortho and para character of the projectile ($H_2$) and the target ($D_2O$) are strictly conserved. Hence, measuring DCSs of HDO/$D_2O$ scattered by normal-$H_2$ and pure para-$H_2$ (95%) separately, we can identify the influence of different rotational states of $H_2$ on the measured differential cross section. The selection and means of measuring the rotational quantum states of HDO, $D_2O$, or $H_2$ are described below, in Sec. II B.

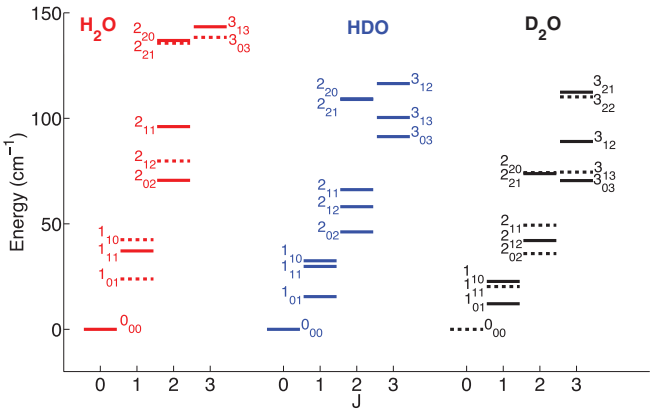


FIG. 1. Rotational energy levels of the three isotopologues of water, for $E < 150$ $cm^{-1}$. Levels are labelled by $J_{K_aK_c}$. Ortho levels ($H_2O$, $K_a + K_c$ odd; $D_2O$, $K_a + K_c$ even) are depicted in dashed lines.

### B. Procedures

Experimental conditions are the same as the one described in our previous papers.[22,23] We will briefly mention them here along with the details of minor modifications adopted for this experiment. HDO is prepared by mixing equal amounts of $H_2O$ with $D_2O$. Rapid conversions take place to convert 50% of the mixture to HDO and the remaining 25% each will exist as $H_2O$ and $D_2O$. Experiments concerning $D_2O$ were conducted the same way, so that spectroscopic detection and mass selection distinguish the two deuterated species.

One bar of Ar is bubbled through the mixture of $H_2O$ and $D_2O$ at room temperature and carries 2.5% of it along to form a molecular beam. We use a Jordan valve for the HDO beam and a Jordan valve or a liquid nitrogen cooled General valve is used for the $H_2$ beam. Both molecular beams pass through skimmers of aperture diameter 3 mm, positioned 3 cm away from the valve nozzle. The HDO/$D_2O$ and pure $H_2$ beams cross each other at a fixed angle of 90° as shown in Fig. 2. HDO molecules, after collision with $H_2$, are ionized using a pulsed dye laser with wavelength around 248 nm. We use (2+1) resonance enhanced multiphoton ionization (REMPI) of HDO, where two photons resonantly excite HDO molecules to the $C^1B_1$ ($v = 0$) state, and the third photon will ionize the molecule.[31] Radiation around 248 nm is produced by a dye laser system (Lambda Physik ScanMate) using Coumarin 307 dye, pumped by 355 nm output from a Nd:YAG laser (Contiuum Powerlite 9010). Radiation at the dye fundamental wavelength was frequency doubled using a BBO crystal to produce 248 nm light. In this work, the laser

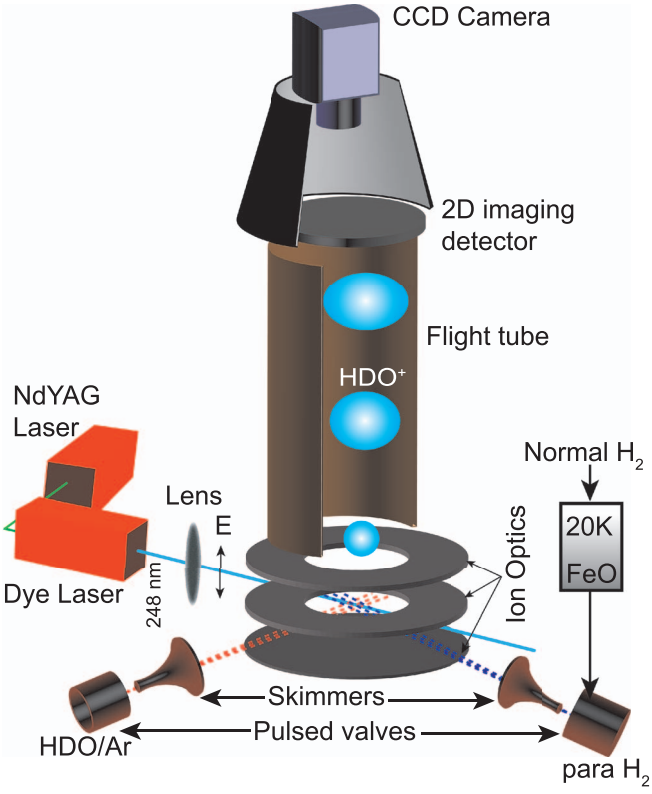


FIG. 2. Schematic of the cross beam VMI setup showing two molecular beams crossing at the center of imaging ion optics.

system is operated at 10 Hz repetition rate with pulse energies of 3-4 mJ. A spherical lens of 20 cm focal length is used to focus the ionization laser within the VMI lens, where the two molecular beams cross each other. The laser beam crosses the molecular beams at an angle of 45° with the HDO/$D_2O$ beam. We used VMI to detect REMPI-ionized $HDO^+$ ions. A potential difference applied to the ion optics plates of the VMI setup projects the evolving Newton sphere of $HDO^+/D_2O^+$ ions to a two-dimensional micro-channel plate detector. The complete detector assembly consists of two micro-channel plates (MCP), a phosphor screen and a CCD camera (Pixel fly). During the experiment, the MCP is turned on only for a short duration using a voltage pulse of length 90 ns, which allows us to separate HDO or $D_2O$ mass by its time-of-flight from other species present in the molecular beam that can be ionized by the same laser wavelength.

The procedure for spectroscopic detection of $D_2O$ rotational states are identical, except for tuning to the relevant resonances.[31]

To measure the state-to-state differential cross sections, it is important to produce rotationally cold molecules in the beam. Supersonic expansion of the molecular beam produces HDO in the lower two rotational levels $0_{00}$ (95%) and $1_{01}$ (5%) in the electronic and vibrational ground state of the molecule. For $D_2O$, around 97% ortho and 86% para population is in the lowest $0_{00}$ and $1_{01}$ state, respectively.

However, it is not possible to efficiently cool $H_2$ in a supersonic expansion due to its large separation of rotational states. Therefore, we used a modified General valve with a gas flow cooling system to cool the valve nozzle. A continuous flow of nitrogen gas through a copper tube that passes through a liquid nitrogen bath decreases the temperature of the valve nozzle. During experiment, this nozzle temperature was kept at 200 K, which decreases the rotational population of $H_2$ via repetitive collisions with the nozzle wall. Nozzle and rotational temperatures of $H_2$ molecular beam and the corresponding measured rotation populations are shown in Table I.

TABLE I. Nozzle and rotational temperatures of $H_2$ molecular beam and the corresponding measured rotational populations.

| | Normal-$H_2$ | | Para-$H_2$ (90 ± 5%) | |
|---|---|---|---|---|
| Nozzle temperature (K) | 320 | 200 | 320 | 200 |
| Temperature of $H_2$ (K) | 220 ± 10 | 170 ± 10 | 220 ± 10 | 170 ± 10 |
| $J = 0$ abundance (%) | 17 ± 1 | 20 ± 1 | 61 ± 2 | 73 ± 3 |
| $J = 1$ abundance (%) | 72 ± 1 | 74.0 ± 0.3 | 10.0 ± 0.1 | 10.0 ± 0.1 |
| $J = 2$ abundance (%) | 8 ± 1 | 5 ± 1 | 29 ± 2 | 17 ± 3 |
| $J > 2$ abundance (%) | 3 ± 1 | 1.0 ± 0.3 | <1 | <1 |

Generally, at low temperatures, ortho- to para-$H_2$ conversion takes place naturally, but the rate is extremely slow,[33] if no magnetic catalyst like iron oxide is used. The mechanism for ortho-para conversion is well known.[33] We employed an experimental method that produces para-$H_2$ for laboratory use with high efficiency at low cost. Iron oxide catalyst is used at a temperature near liquid He for the conversion of normal- to para-$H_2$. The ortho-para conversion setup (Fig. 3) consists of a hollow stainless steel cylinder of diameter 20 mm joined with a copper cylinder at one end. A small stainless steel tube that goes through the hollow cylinder carries $H_2$ gas and opens at the copper cylinder which is the main reservoir of $H_2$ during ortho-to-para conversion. Iron oxide is placed inside the copper cylinder as a catalyst. A temperature sensor is mounted at the joint of two cylinders through a small opening in the hollow stainless steel housing. Connections for the temperature sensor come out along with the small stainless steel tube at the top of the hollow cylinder. The whole assembly is lowered into a standard liquid He Dewar. The copper cylinder is kept just above the liquid He level in the Dewar so that its temperature is around the liquefaction temperature of $H_2$ (20 K). Immersing the copper cylinder too deep inside the liquid He

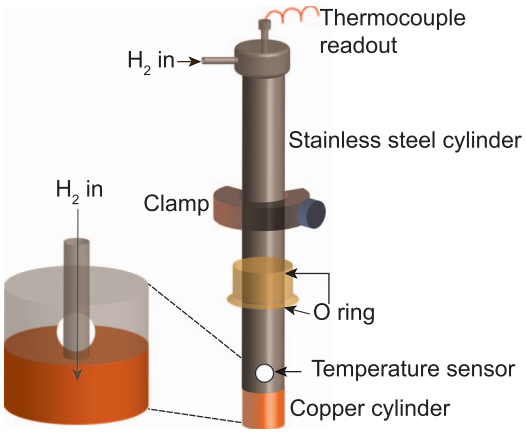


FIG. 3. Experimental setup for normal- to para-$H_2$ conversion.

solidifies $H_2$ and hinders the ortho-para conversion process. The percentage of para-$H_2$ in the sample is measured with high accuracy using REMPI of $H_2$.[22,34] Results are given in Table I.

## III. THEORETICAL COMPUTATION

The experimental differential cross sections measured in this work are compared with theoretical computations. The interaction PES derives from the full nine-dimensional (9D) $H_2O - H_2$ PES computed by Valiron *et al.*[19] Since that PES is explicitly dependent on all intra-molecular coordinates, it is possible to average the 9D PES over the ground-state wave function of the various isotopologues of the $H_2O - H_2$ system. Here, we use the PES averaged either on the $D_2O - H_2$ or on the $HDO - H_2$ ground state vibrational function, as described in Ref. 35 for $D_2O$ or in Ref. 30, for HDO. While the symmetry of $D_2O$ is the same as the symmetry of $H_2O$ (apart from the ortho $\leftrightarrow$ para inversion, (Fig 1)), the principal inertia axes of HDO are tilted (see Sec. II A above), and the PES had to be adapted. Computations of the DCS here employ the PES as just defined, which are subsequently fitted on a spherical harmonic basis adapted for the quantum scattering program. We use the MOLSCAT scattering program,[36] with all internal parameters standard, at ITYPE = 4. In a first step the relevant $S_{i,f}(E)$ matrices connecting initial and final rotational levels $i$ and $f$ are computed. Then the differential cross section $d\sigma/d\theta$ are formed, using the same expression as in Ref. 22.

Convergence of the DCS was carefully monitored, as the total inelastic cross section may be converged, while the DCS may be not, especially so for forward and/or backward scattering. The convergence with respect to basis set was obtained with $J(\mathrm{HDO}) \leq 10$, for energy levels less then 1350 $cm^{-1}$. We summed partial waves up to $L \lesssim 70$ (partial wave angular momentum). Similar conditions were used for $D_2O$ computations, with partial waves summations up to $J \lesssim 70$.

In order to properly simulate the experimental conditions, we used many initial conditions, all with the same relevant collision energies. For HDO–$H_2$, the collision energy was 440 $cm^{-1}$ at the low temperature nozzle of $H_2$ and 580 $cm^{-1}$ at the room temperature nozzle of $H_2$. For $D_2O$, we use 584 $cm^{-1}$. In all instances, as was also noticed for the various $H_2O$–$H_2$ DCS, in the energy range of the experiments, far above all the resonances, the DCS shape varies little with collision energy. The comparison experiment-theory relies on the proper weighting of the different channels contributing to an experimental DCS. The composition of the $H_2$ beam is monitored by appropriate REMPI measurements, see Table I. The HDO beam is considered to be pure ground-state HDO ($0_{00}$). For $D_2O$, because of the reduced spacing between the first rotational levels, we considered the possibility of the $D_2O$ initial beam to be populated, either purely with the ground state (Theory 1 in Fig. 7) or else with some population of the first excited states (Theory 2 in Fig. 7). The best adjustments were found at 20% of $1_{11}$ in the $0_{00}$ beam and 15% of $1_{10}$ in the $1_{01}$ beam. Theory (1) is close to the 97% $0_{00}$ beam composition measured experimentally. We simply test the effect of higher state contamination by using the significant 20% of level $1_{11}$ to construct Theory 2. While experiments indicate a different composition of the incoming $D_2O$ beam, the theoretical simulation tend to produce less pure beams, in particular, for $D_2O$. One must bear into account, however, that the difference occurs on the one hand, with a largely undermeasured forward scattering, and for very small actual values of the sideways and backward DCS scattering, on the other hand. The actual composition of the beams cannot actually be extracted from our computations, which remain indicative in this respect. Also, for those sections connecting water excited states, only $j(H_2) = 0, 1$ were considered.

TABLE II. Total computed cross sections (in $Å^2$, exponent in the parenthesis), for the indicated rotational transitions of HDO colliding with $H_2$. Only observed channels are included. Other values may be obtained from the authors.

| $J$(HDO) | $J(H_2)$ | $\sigma(440\,cm^{-1})$ | $\sigma(580\,cm^{-1})$ |
|---|---|---|---|
| $0_{00} \rightarrow 1_{11}$ | $0 \rightarrow 0$ | 6.62(0) | 7.17(0) |
| | $0 \rightarrow 2$ | 2.31(−2) | 7.43(−2) |
| | $2 \rightarrow 0$ | 1.89(−1) | 2.58(−1) |
| | $2 \rightarrow 2$ | 1.41(+1) | 1.16(+1) |
| | $1 \rightarrow 1$ | 1.31(+1) | 1.27(+1) |
| $0_{00} \rightarrow 2_{12}$ | $0 \rightarrow 0$ | 4.43(−1) | 3.71(−1) |
| | $0 \rightarrow 2$ | 4.29(−3) | 2.44(−2) |
| | $2 \rightarrow 0$ | 1.25(−1) | 1.53(−1) |
| | $2 \rightarrow 2$ | 1.79(0) | 1.51(0) |
| | $1 \rightarrow 1$ | 1.82(0) | 1.77(0) |
| $0_{00} \rightarrow 2_{21}$ | $0 \rightarrow 0$ | 1.19(−3) | 1.65(−3) |
| | $0 \rightarrow 2$ | Closed | 3.43(−3) |
| | $2 \rightarrow 0$ | 2.47(−2) | 2.55(−2) |
| | $2 \rightarrow 2$ | 2.04(−1) | 1.89(−1) |
| | $1 \rightarrow 1$ | 1.88(−1) | 0.18(0) |
| $0_{00} \rightarrow 2_{20}$ | $0 \rightarrow 0$ | 9.36(−1) | 1.03(0) |
| | $0 \rightarrow 2$ | Closed | 1.49(−2) |
| | $2 \rightarrow 0$ | 3.14(−1) | 3.83(−1) |
| | $2 \rightarrow 2$ | 1.85(0) | 3.49(0) |
| | $1 \rightarrow 1$ | 4.04(0) | 3.99(0) |

The total cross sections of all the relevant channels are given in Tables II and III. From the measured composition of the $H_2$ beams (Table I), the DCSs are weighted, giving the theoretical values given in Figs. 5–7.

## IV. RESULTS

### A. Differential cross sections

Figure 4 shows an experimental raw image of HDO scattered by normal-$H_2$. Each velocity mapped image was measured by accumulating $HDO^+$ ions for around 8000 laser shots. After every 100 laser shots, the secondary ($H_2$) beam was delayed by 1 ms with respect to the timing of laser to record the hot HDO molecules present in the primary beam. Later on, this primary beam signal is subtracted to remove the parent beam contribution present in the forward scattering part of the velocity mapped image.

Differential or integral cross section measurements in a crossed beam experiment using a focused nanoseconds pulse length dye laser imply that molecular collisions taking place during a very large temporal profile of two molecular beams are probed by a short time duration laser pulse, in a finite

TABLE III. Same as Table II, for ortho-$D_2O$ and para-$D_2O$ transitions. $\sigma_o$ and $\sigma_p$ indicate the total computed cross sections for ortho- and para-$D_2O$, respectively.

| $J$(ortho-$D_2O$) | $J$(para-$D_2O$) | $J(H_2)$ | $\sigma_o(584\,cm^{-1})$ | $\sigma_p(584\,cm^{-1})$ |
|---|---|---|---|---|
| $0_{00} \rightarrow 1_{11}$ | $1_{01} \rightarrow 1_{10}$ | $0 \rightarrow 0$ | 8.44(0) | 4.27(0) |
| | | $0 \rightarrow 2$ | 1.10(−1) | 9.47(−2) |
| | | $2 \rightarrow 0$ | 2.85(−1) | 1.56(−1) |
| | | $2 \rightarrow 2$ | 1.22(+1) | 6.68(0) |
| | | $1 \rightarrow 1$ | 1.37(+1) | 7.54(0) |
| $0_{00} \rightarrow 2_{02}$ | $1_{01} \rightarrow 2_{12}$ | $0 \rightarrow 0$ | 1.96(0) | 4.69(0) |
| | | $0 \rightarrow 2$ | 1.46(−1) | 8.85(−2) |
| | | $2 \rightarrow 0$ | 5.08(−1) | 2.17(−1) |
| | | $2 \rightarrow 2$ | 5.70(0) | 7.42(0) |
| | | $1 \rightarrow 1$ | 6.32(0) | 8.20(0) |
| $0_{00} \rightarrow 2_{20}$ | $1_{01} \rightarrow 2_{21}$ | $0 \rightarrow 0$ | 1.26(+1) | 7.17(−1) |
| | | $0 \rightarrow 2$ | 3.69(−2) | 3.11(−2) |
| | | $2 \rightarrow 0$ | 2.77(−1) | 1.32(−1) |
| | | $2 \rightarrow 2$ | 3.73(0) | 2.22(0) |
| | | $1 \rightarrow 1$ | 3.96(0) | 2.35(0) |

detection volume. A density-to-flux transformation is needed to extract the differential cross section from the velocity mapped images of scattered molecules. This conversion is described in detail in Ref. 24.

Using the two different $H_2$ beam conditions differing in temperature and para-$H_2$ content (see Table I), and performing the density-to-flux conversion, we present the various differential cross sections in Figs. 5–7, both for HDO and $D_2O$.

Figures 5 and 6, show a comparison of experimental and calculated differential cross sections of HDO scattered by normal- and para-$H_2$ at collision energy 580 $cm^{-1}$ and 440 $cm^{-1}$. In all presented comparison theory/ experiments (HDO and $D_2O$), the normalization was chosen to be the value of the DCSs at a deflection angle of 60°. Similarly, Fig. 7 compares theoretical and experimental results for DCS of both ortho- and para-$D_2O$, scattering with normal-$H_2$ (320 K nozzle), under the same conditions as the HDO scattering (collision energy, 584 $cm^{-1}$).

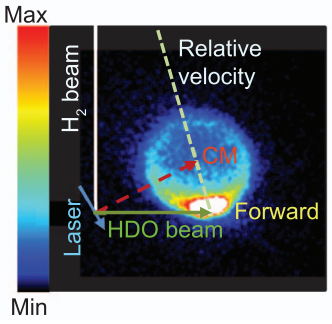


FIG. 4. Raw $HDO^+$ image, showing the molecular beam and laser geometry in the laboratory and center of mass frame. The presented $HDO^+$ image is a 2D projection of the Newton sphere formed by HDO collisions with normal-$H_2$, for the $0_{00} \rightarrow 1_{11}$ transition. "CM" refers to the position of the center of mass vector. Forward direction of scattering is defined by the direction of HDO molecules before collision in the center of mass frame.

### B. State-to-state relative integral cross sections

Integral cross sections of HDO scattered by normal-$H_2$ are presented in Fig. 8. The experimental total cross sections are extracted from the HDO ion images by integrating the scattering signal at all scattering angles. To apply the density-to-flux transformation, the relative cross sections are weighted by the intensity of the corresponding "imsim" simulated image that contains the excess intensity due to slow molecules preferentially ionized in the lab frame. Afterwards, the total intensities of the experimental images of HDO at measured rotational states are weighted according to the line strengths of their corresponding REMPI transition. The error bars in the graph present the uncertainties in the repeatability of the measurements. Absolute values of the DCS and ICS cannot be measured in our experiment because the density of molecules in the molecular beam is unknown. Hence, total cross sections from both experiment and theory are normalized to the $0_{00} \rightarrow 1_{11}$ transition. A discussion of the various propensity rules is put forward in Sec. V.

## V. DISCUSSION AND CONCLUSION

Before comparing experiment and theory for state-to-state differential cross sections in HDO–$H_2$, it is useful to summarize the results of Ref. 30, which describes the differences in collision rates for HDO versus $H_2O$/$D_2O$ collisions with hydrogen. As described in Ref. 30, the substitution of a H atom by a D atom in HDO both breaks the $C_{2v}$ symmetry of the molecule and removes the ortho-para distinction. Inspecting Fig. 1, one might thus expect that the ortho-para forbidden $0_{00} \rightarrow 1_{01}$ excitation in $H_2O$ would be strong in HDO, especially considering its low energy difference. However, radiative dipolar transition rules dominate in water-hydrogen collisions. These rules are affected by the changes between HDO and $H_2O$ ($D_2O$) because of the disappearance of the ortho/para modifications and by the tilting of the dipole with respect to the principal inertia axes. Let us recall that the dipole-allowed transitions for $H_2O$ (and $D_2O$) are of the type: $\Delta J = 0, \pm1$, $\Delta K_a = \pm1, \pm3, \ldots$, and $\Delta K_c = \pm1, \pm3, \ldots$. For HDO, because of the misalignment of the dipole, the $\Delta K_a = 0, \pm2, \ldots$ becomes dipole-authorized. Hence, all transitions of HDO from $J = 0$ to 1 are possible, with the $0_{00} \rightarrow 1_{11}$ clearly favored. For all three molecules propensity rules are also influenced by intramolecular rotational alignment, which is described in detail by Nesbitt and co-workers.[37] These rules favor $\Delta J = |\Delta K_a|$ or $|\Delta K_c|$. This is clearly seen for the $J = 0 \rightarrow J = 2$ transitions, where the theoretical total cross sections of the $0_{00} \rightarrow 2_{02}$, $2_{12}$, $2_{11}$, $2_{21}$, $2_{20}$ transitions follow the characteristic pattern (at a collision energy of 440 $cm^{-1}$ and with $J(H_2) = 0$): $\sigma \sim 6$, 0.02, 0.0001, 0.001, 1.6 $Å^2$. A classical argument for this propensity rules appeals to the stability of rotation around the $a$ and $c$ axes, while the $b$ axis is unstable favoring states with the angular momentum aligned with those two axes. While the relative strengths of integral state-to-state cross sections thus change somewhat due to D substitution, the shapes of the differential cross sections for individual state-to-state excitations for HDO–$H_2$ collisions shown in Figs. 5 and 6 look quite similar to those for

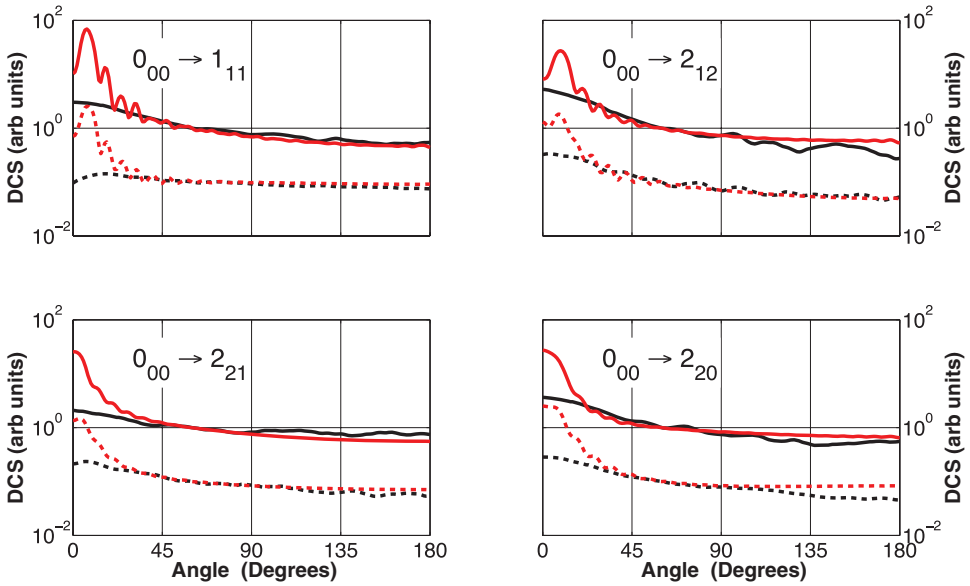


FIG. 5. Comparison of experiment and theory for DCS for HDO scattered by low temperature $H_2$ ($T = 200$ K nozzle). Theory, red; experimental, black. Normal-$H_2$, full lines. Para-$H_2$, dashed lines. DCSs for para-$H_2$ are divided by 10 for clarity. The HDO rotational transition is indicated in each panel. We use log scales to magnify the small disagreement between experiment and theory in the sideways and backward directions.

$H_2O$–$H_2$ collisions.[22] Finally, it must be underlined that for small total sections, such as the $2_{21}$ final state, experimental errors because of very weak contamination with other scattering event, e.g., because of the presence of other initial states than $0_{00}$ in the beam, may change drastically the observed cross section.

### A. Experiment-theory comparison

In a manner similar to our earlier studies on $H_2O$–$H_2$ DCSs, the agreement between experiment and theory is excellent in nearly all cases presented here, for all angles $30^\circ \lesssim \theta \leq 180^\circ$.

There are larger uncertainties in the forward part of the DCS from experiment (Fig. 9) due to final states present in the parent beam (HDO, before collision), which results in problems with background subtraction. To verify if this is the reason behind the poor agreement between the DCSs from theory and experiment at lower scattering angles, we compared DCSs from experiment without HDO beam background subtraction with the DCSs from the calculation. The theoretical DCSs still largely overestimate the cross sections in the forward scattering direction (see Fig. 9). We carefully checked the balance between the forward and backward directions in all theoretical DCSs. Overall convergence is obtained for partial waves with total angular momentum $L \lesssim 45$. nevertheless, all DCSs are summed up to $L = 80$, ensuring an excellent

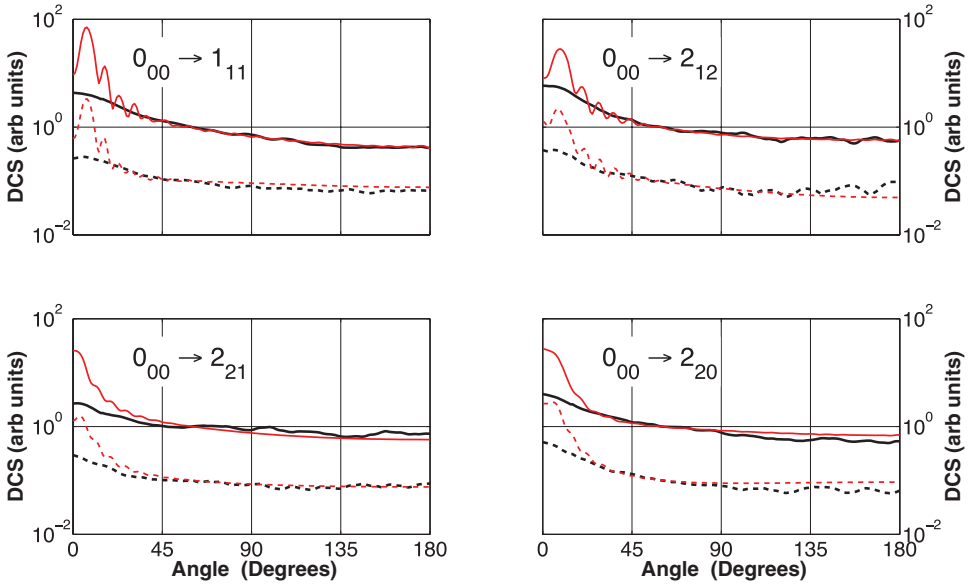


FIG. 6. Same as Fig. 5, but room temperature $H_2$ ($T = 320$ K nozzle).

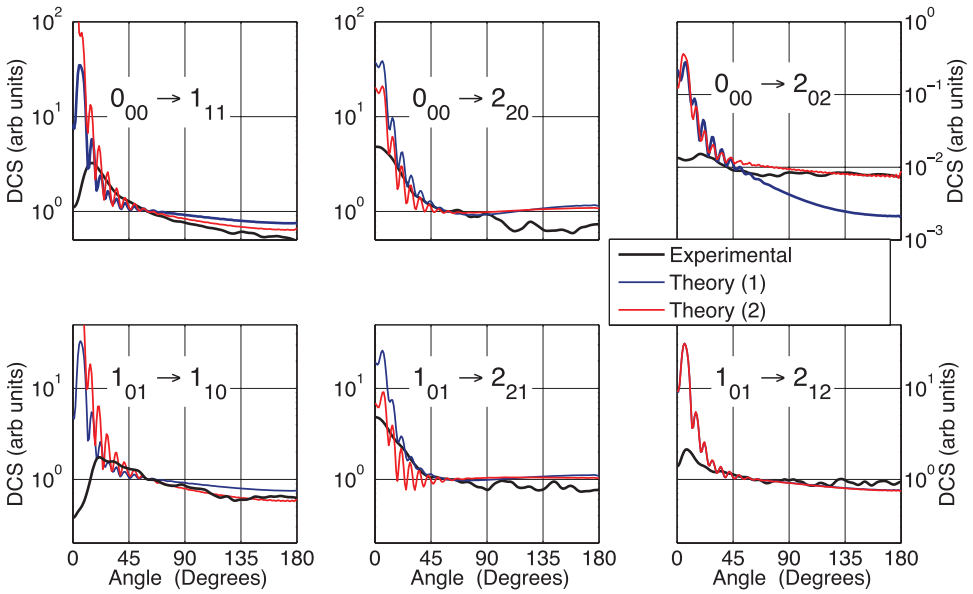


FIG. 7. Comparison of experiment and theory for DCS of $D_2O$ scattered by room-temperature normal-$H_2$. Experiment, black. Theory(1) (blue line): Only the ground state of the incoming beam is taken into account. Theory(2) (red line): the incoming beam has either 20% of level $1_{11}$ (ortho-$D_2O$) or 15% of $1_{10}$ (para-$D_2O$) in its composition. Both curves are identical for the $1_{01} \rightarrow 2_{12}$ transition. We use log scales to magnify the small disagreement between experiment and theory in the sideways and backward directions.

convergence. All theoretical uncertainties result, in practice, to the imperfections at very long distance of the PES.

We could similarly rule out "event counting" problems that might count overlapped ion events as a single event on the detector, by using a"sequence summing" method, which avoids possible under-counting problem and compared it with the results obtained from the "event counting." Finally, the $H_2$ beam composition is fully taken into account in the theoretical estimates. Another uncertainty in the experimental DCSs may arise from the velocity distribution and angular spread of the molecular beams that cause a spread in the center of mass and relative velocity vectors, which, consequently, lower the angular resolution of the image. The angular spread in the HDO/$D_2O$/$H_2$ beam is 5.6°. The speed ratios (v/Δv) of HDO and $H_2$ beams are 10 and 6, respectively. As the "imsim" simulation uses the experimental parameters: molecular speed distribution and the angular divergence of both the primary and secondary beams to simulate an image, we can approximately estimate the angular resolution of the DCSs by using this simulation. The angular resolution of the experimental DCSs for HDO scattered by $H_2$ in the forward direction (0°–30°) is 15°. This means that we cannot resolve the narrow peaks in the DCS if they exist below 15° of separation. In order to approximate the error in the comparison, the theoretical DCSs can be convoluted with the blurring due to experimental angular resolution. The green curve in Fig. 9 is obtained by simulating the theoretical DCS using the experimental apparatus function, and hence gives an estimate of the blurring due to velocity and angular spread in the molecular beams. It shows that the poor angular resolution of experiments in

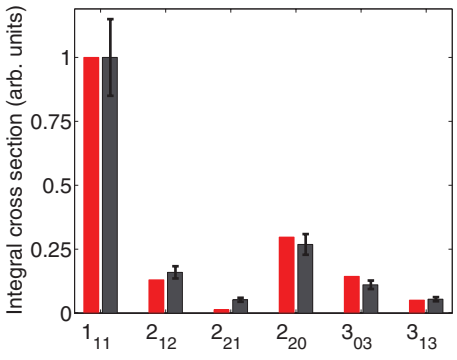


FIG. 8. Relative integral cross sections obtained from experiment (black) and quantum mechanical calculations (red) for collisions of HDO with normal-$H_2$ (320 K nozzle). The experimental relative cross sections are normalized to the calculated cross sections at the $1_{11}$ state. The experimental uncertainty is ∼15%.

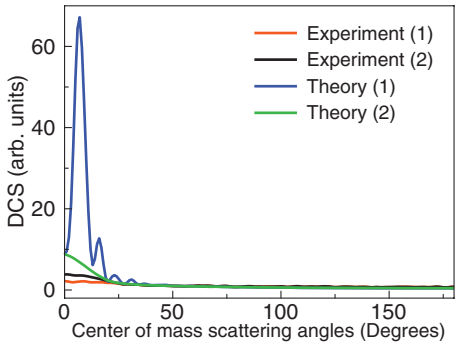


FIG. 9. Differential cross sections obtained from experiment and theory for collisions of HDO ($0_{00}$-$1_{11}$ transition) with normal-$H_2$ (320 K nozzle). Experiment (1): The DCS of HDO obtained by subtracting the signal due to $1_{11}$ state population in the HDO beam before collision with $H_2$. Experiment (2): The DCS of HDO without HDO parent beam subtraction. Theory (1) represents the DCS from theory. Theory (2): "Imsim" simulation result of Theory (1) using experimental apparatus function. It gives an estimate of the blurring due to velocity and angular spread in the molecular beams. The angular resolution of the experimental DCSs in the forward direction (0°–30°) is 15°. Normalization is at the values of the DCSs at 60°.

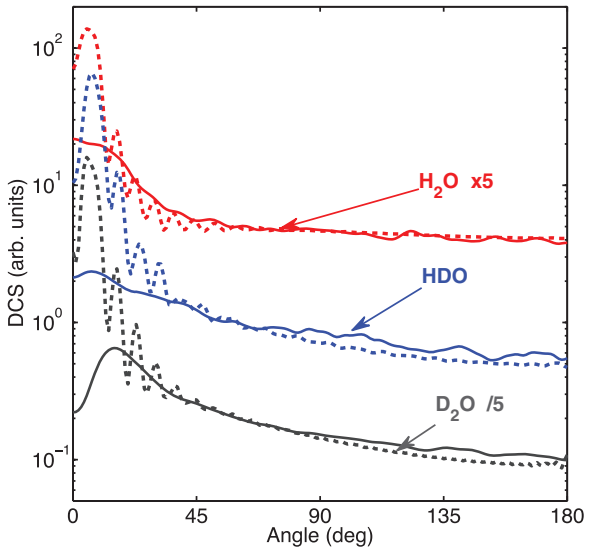


FIG. 10. For three isotopologues $H_2O$, HDO, and $D_2O$, comparison of experiment (solid line) and theory (dashed line) for the $0_{00} \rightarrow 1_{11}$ transition.

the forward direction can significantly contribute to the observed discrepancy in the DCS from theory and experiment. Moreover, the rather large discrepancy in forward scattering, increasing from $H_2O$ to $D_2O$, then to HDO (Fig. 10), must be understood by both a critical view on the density-to-flux conversion of the experiment and by a proper reappraisal of the long range PES between water and hydrogen. Note, however, that because of the $\sin\theta$ term in the total cross section expression

$$\sigma_{f\leftarrow i}(E) = 2\pi \int_0^{\pi} d\sigma_{f\leftarrow i}(E)/d\theta \, \sin\theta \, d\theta \quad , \qquad (3)$$

the agreement in the total cross sections remains very good – as Fig. 8 shows – and largely within all the other error ranges for any astrophysical observation. The forward discrepancy cannot consequently hinder the astrophysical modeling, all the more considering that pressure broadening cross sections show a quantitative agreement between theory and experiment, on an absolute scale.[27,28,38]

## B. Conclusion

We have presented state-to-state DCSs for rotationally inelastic scattering of HDO and $D_2O$ by normal- and para- $H_2$ at collision energies of 580 and 440 $cm^{-1}$. Relative integral cross sections of HDO scattered by normal-$H_2$ at collision energy 580 $cm^{-1}$ are obtained by integrating the DCSs for different final states measured while keeping the experimental conditions the same during measurements. Both the DCSs and integral cross sections from experiment were compared with calculated cross sections. We found a good agreement between experimental and theoretical DCSs of HDO scattered by normal- and para-$H_2$ except at forward scattering directions (0°–30°) where theory largely overestimates and experiments may underestimate the cross sections for all the transitions measured in our experiment. Furthermore, we found a very decent agreement between theory and experiment for integral cross sections of HDO scattered by normal-$H_2$ (320 K nozzle). This reasonable agreement of DCSs and ICSs once again confirms the accuracy of the potential for $H_2O$–$H_2$, by using a completely different set of rotational transitions from $H_2O$. Similar conclusions may be drawn from the $D_2O$ experiments. The disagreement of the DCS from theory and experiment in the very forward direction that we also found for $H_2O$–$H_2$ scattering system repeats here. We found that the poor angular resolution of experiments in the forward direction can significantly contribute to the observed discrepancy in the DCS from theory and experiment. Therefore, the discrepancy in forward scattering must be understood by both a critical view on the determination of experimental angular resolution, intensity-to-flux conversion of the experiment and by a proper reappraisal of the very long range PES between water and hydrogen. Extending experiments and theory on both the low energy end, to probe the backward scattering better, and to the high energy end, to look for stronger elastic effects and also the beginning of vibration transitions, would put a very stringent test on the $H_2O$–$H_2$ full 9D potential energy surface.

## ACKNOWLEDGMENTS

L.W. thanks the NWO as well as the COST program CM 085: "The Chemical Cosmos" for partial support or travel funding. Computations were performed at the Centre de Calcul Intensif of the Observatoire de Grenoble. Part of this work is funded by the Van Gogh Dutch-French exchange fund. The Nijmegen group acknowledges support by the NWO Dutch Astrochemistry Network and the NWO-CW ECHO Grant No. 700.58.029. The authors thank A. Faure, Y. Scribano, and A. van der Avoird for fruitful discussions.

[1]E. F. van Dishoeck, L. E. Kristensen, A. O. Benz, E. A. Bergin, P. Caselli, J. Cernicharo, F. Herpin, M. R. Hogerheijde, D. Johnstone, R. Liseau *et al.*, Publ. Astron. Soc. Pac. **123**, 138 (2011); e-print arXiv:1012.4570.
[2]N. Flagey, P. F. Goldsmith, D. C. Lis, and PRISMAS Team, *American Astronomical Society Meeting Abstracts*, American Astronomical Society Vol. 219 (American Astronomical Society, 2012), p. 302.01.
[3]G. Santangelo, B. Nisini, T. Giannini, S. Antoniucci, M. Vasta, C. Codella, A. Lorenzani, M. Tafalla, R. Liseau, E. F. van Dishoeck *et al.*, Astron. Astrophys. **538**, A45 (2012); e-print arXiv:1111.6016.
[4]M. R. Hogerheijde, E. A. Bergin, C. Brinch, L. I. Cleeves, J. K. J. Fogel, G. A. Blake, C. Dominik, D. C. Lis, G. Melnick, D. Neufeld *et al.*, Science **334**, 338 (2011); e-print arXiv:1110.4600.
[5]S. Viti, I. Jimenez-Serra, J. A. Yates, C. Codella, M. Vasta, P. Caselli, B. Lefloch, and C. Ceccarelli, Astrophys. J. Lett. **740**, L3 (2011).
[6]A. Coutens, C. Vastel, E. Caux, C. Ceccarelli, and Herschel Chess Team, in *Proceedings of the International Astronomical Union Symposium*, IAU Vol. 280 (International Astronomical Union, 2011), p. 139.
[7]F. P. Helmich, E. F. van Dishoeck, and D. J. Jansen, Astron. Astrophys. **313**, 657 (1996).
[8]L. Loinard, A. Castets, C. Ceccarelli, E. Caux, and A. G. G. M. Tielens, Ap. J. **552**, L163 (2001).
[9]E. Dartois, W.-F. Thi, T. R. Geballe, D. Deboffle, L. d'Hendecourt, and E. van Dishoeck, Astron. Astrophys. **399**, 1009 (2003).
[10]B. Parise, E. Caux, A. Castets, C. Ceccarelli, L. Loinard, A. G. G. M. Tielens, A. Bacmann, S. Cazaux, C. Comito, F. Helmich *et al.*, Astron. Astrophys. **431**, 547 (2005); e-print arXiv:astro-ph/0410619.
[11]C. Ceccarelli, A. Bacmann, A. Boogert, E. Caux, C. Dominik, B. Lefloch, D. Lis, P. Schilke, F. van der Tak, P. Caselli *et al.*, Astron. Astrophys. **521**, L22 (2010).
[12]C. Vastel, C. Ceccarelli, E. Caux, A. Coutens, J. Cernicharo, S. Bottinelli, K. Demyk, A. Faure, L. Wiesenfeld, Y. Scribano *et al.*, Astron. Astrophys. **521**, L31 (2010); e-print arXiv:1007.4410.

[13]J. K. Jørgensen and E. F. van Dishoeck, Ap. J. **725**, L172 (2010); e-print arXiv:1011.2970.
[14]F.-C. Liu, B. Parise, L. Kristensen, R. Visser, E. F. van Dishoeck, and R. Güsten, Astron. Astrophys. **527**, A19 (2011); e-print arXiv:1101.3880.
[15]A. Coutens, C. Vastel, E. Caux, C. Ceccarelli, S. Bottinelli, L. Wiesenfeld, A. Faure, Y. Scribano, and C. Kahane, Astron. Astrophys. **539**, A132 (2012).
[16]B. Parise, C. Ceccarelli, A. G. G. M. Tielens, A. Castets, E. Caux, B. Lefloch, and S. Maret, Astron. Astrophys. **453**, 949 (2006); e-print arXiv:astro-ph/0603135.
[17]H. M. Butner, S. B. Charnley, C. Ceccarelli, S. D. Rodgers, J. R. Pardo, B. Parise, J. Cernicharo, and G. R. Davis, Ap. J. **659**, L137 (2007).
[18]A. Faure, L. Wiesenfeld, Y. Scribano, and C. Ceccarelli, Mon. Not. R. Astron. Soc. **420**, 699 (2012).
[19]P. Valiron, M. Wernli, A. Faure, L. Wiesenfeld, C. Rist, S. Kedžuch, and J. Noga, J. Chem. Phys. **129**, 134306 (2008).
[20]A. Faure, N. Crimier, C. Ceccarelli, P. Valiron, L. Wiesenfeld, and M. L. Dubernet, Astron. Astrophys. **472**, 1029 (2007); e-print arXiv:0708.0345.
[21]A. T. J. B. Eppink and D. H. Parker, Rev. Sci. Instrum. **68**, 3477 (1997).
[22]C.-H. Yang, G. Sarma, D. H. Parker, J. J. Ter Meulen, and L. Wiesenfeld, J. Chem. Phys. **134**, 204308 (2011); e-print arXiv:1104.2715.
[23]C.-H. Yang, G. Sarma, J. J. Ter Meulen, D. H. Parker, G. C. McBane, L. Wiesenfeld, A. Faure, Y. Scribano, and N. Feautrier, J. Chem. Phys. **133**, 131103 (2010).
[24]C.-H. Yang, G. Sarma, J. J. ter Meulen, D. H. Parker, U. Buck, and L. Wiesenfeld, J. Phys. Chem. A **114**, 9886 (2010).
[25]L. Wiesenfeld and A. Faure, Phys. Rev. A **82**, 040702 (2010); e-print arXiv:1009.1699.
[26]M. J. Dick, B. J. Drouin, and J. C. Pearson, Phys. Rev. A **81**, 022706 (2010).
[27]B. J. Drouin, J. C. Pearson, L. Wiesenfeld, and A. Faure, in *Proceedings of the 66th International Symposium On Molecular Spectroscopy*, 2011.
[28]B. Drouin and L. Wiesenfeld, Phys. Rev. A **86**, 022705 (2012).
[29]M.-L. Dubernet and A. Grosjean, Astron. Astrophys. **390**, 793 (2002).
[30]L. Wiesenfeld, Y. Scribano, and A. Faure, Phys. Chem. Chem. Phys. **13**, 8230 (2011).
[31]C.-H. Yang, G. Sarma, J. J. ter Meulen, D. H. Parker, and C. M. Western, Phys. Chem. Chem. Phys. **12**, 13983 (2010).
[32]See http://spec.jpl.nasa.gov/ftp/pub/catalog/catdir.html for Jpl data base.
[33]Y. Milenko, R. Sibileva, and M. Strzhemechny, J. Low Temp. Phys. **107**, 77 (1997).
[34]M. J. J. Vrakking, A. S. Bracker, T. Suzuki, and Y. T. Lee, Rev. Sci. Instrum. **64**, 645 (1993).
[35]Y. Scribano, A. Faure, and L. Wiesenfeld, J. Chem. Phys. **133**, 231105 (2010).
[36]J. M. Hutson and S. Green, MOLSCAT computer code, version 14 (distributed by Collaborative Computational Project No. 6 of the Engineering and Physical Sciences Research Council UK), 1994.
[37]W. B. Chapman, A. Kulcke, B. W. Blackmon, and D. J. Nesbitt, J. Chem. Phys. **110**, 8543 (1999).
[38]A. Faure, L. Wiesenfeld, B. Drouin, and J. Tennyson, "Pressure broadening of water and carbon monoxide transitions by molecular hydrogen at high temperatures," J. Quant. Spectrosc. Radiat. Transf. (published online).